Multiscale study of gas slip flows in nanochannels

Quy Dong To, Thanh Tung Pham, Vincent Brites, Céline Léonard, Guy Lauriat

Multiscale Study of Gas Slip Flows in Nanochannels

Quy Dong To, Thanh Tung Pham, Vincent Brites, Céline Léonard, Guy Lauriat

Laboratoire Modélisation et Simulation Multi Echelle, UMR-CNRS 8208, Université Paris-Est, 5 Boulevard Descartes, Marne-la-Vallée Cedex 2 77454, France

A multiscale modeling of the anisotropic slip phenomenon for gas flows is presented in a tree-step approach: determination of the gas–wall potential, simulation and modeling of the gas–wall collisions, simulation and modeling of the anisotropic slip effects. The den-sity functional theory (DFT) is used to examine the interaction between the Pt–Ar gas–wall couple. This potential is then passed into molecular dynamics (MD) simulations of beam scattering experiments in order to calculate accommodation coefficients. These coefficients enter in an effective gas–wall interaction model, which is the base of efficient MD simulations of gas flows between anisotropic surfaces. The slip effects are quantified numerically and compared with simplified theoretical models derived in this paper. The paper demonstrates that the DFT potential is in good agreement with empirical potentials and that an extension of the Maxwell model can describe anisotropic slip effects due to surface roughness, provided that two tangential accommodation parameters are intro-duced. MD data show excellent agreement with the tensorial slip theory, except at large Kundsen numbers (for example, Kn ’0.2) and with an analytical expression which predicts the ratio between transverse and longitudinal slip velocity components.

Keywords: density functional theory, molecular dynamics, tangential momentum accommodation coefficient, gas–wall collision, anisotropic surfaces, anisotropic slip

1 Introduction

The slip velocity effect at the wall interface becomes important when the Knudsen number is above 10^{-3}. In most problems, the Maxwell slip model is used based on the tangential momentum accommodation coefficient (TMAC), a gas–wall couple constant. The original Maxwell slip theory is isotropic which is not suitable for strongly anisotropic surfaces.

We present a synthesis of our recent works as a multiscale analysis of the anisotropic slip phenomenon which includes three stages: (i) the ab initio determination of a gas–wall interaction potential, (ii) molecular dynamic (MD) computation of the isotropic/anisotropic TMAC coefficients on different surfaces, and (iii) MD simulation of gas flows using an anisotropic surface model and comparison with the slip theory. The interaction between an Ar gas atom and a solid Pt fcc (111) slab is carried out using CRYSTAL 09 software and PBE functional for solids (PBEsol). The ab initio-based results including equilibrium distance and adsorption energy are in good agreement with empirical results in literature. The gas–wall potential is then decomposed to pairwise potentials for MD simulation.

Next, the TMAC coefficients are computed using MD method with the pairwise potential. The gas atoms are projected onto the solid slabs with different arriving angles and relative momentum changes are measured to determine the TMAC coefficients for smooth surfaces and anisotropic surfaces with stripes. The phantom layer technique is used to maintain the bulk solid atoms at constant temperature allowing the study of the temperature effect. The orientation dependency of TMACs is computed and analyzed in comparison with isotropic/anisotropic scattering kernel models.

Finally, we use MD method to simulate gas flows in nanochannel. Instead of describing explicitly the solid atomic wall, an effective anisotropic gas wall collision mechanism with TMAC coefficients determined previously is adopted. A special MD wall boundary condition is proposed to mimic the mechanism. It is shown that the extension of the Maxwell model using two TMAC parameters can describe quite well the anisotropic slip effect in the slip regime.

2 Choice of the Gas–Wall Potential

In our multiscale approach, the first step consists in the determination of the pair potentials necessary to the MD simulations. Most Pt–Ar potentials found in the literature were obtained

[1] Present address: Université d’Evry Val d’Essonne, Laboratoire Analyse et Modélisation pour la Biologie et l’Environnement, LAMBE CNRS UMR 8587, Boulevard F. Mitterrand, Evry Cedex 91025, France.

empirically due to the lack of accurate and efficient ab initio computational method. Consequently, the CRYSTAL 09 [1] code based on the DFT was used to analyze the interaction between an Ar atom and a large three-layer periodic Pt(111) slab [2]. The pseudopotential and the basis sets developed by Doll [3] and Nada et al. [4] are used to describe the Pt and Ar atoms.

To compute the interaction, the Ar atom was placed at the a fcc-hollow site with varying distance z and the resulting energies were fitted by a sum of pairwise functions over all Pt atoms

$$V^{\mathrm{Pt(111)-Ar}}(z) = \sum_i V^{\mathrm{Pt-Ar}}(r_{\mathrm{Pt}_i-\mathrm{Ar}}) \tag{1}$$

where $r_{\mathrm{Pt}_i-\mathrm{Ar}}$ is the distance between a Pt and the Ar atoms.

For most of the pairwise potentials studied in this work, the pairwise interaction can be neglected for $r_{\mathrm{Pt-Ar}} > 8.0$ Å. The convergence of the recomposed potential $V^{\mathrm{Pt(111)-Ar}}(z)$ relative to the number of Pt atoms has been checked, in particular the addition of a fourth layer has a negligible contribution in the sum of Eq. (1).

Figure 1 and Table 1 present the Pt(111)–Ar potential computed by the ab initio approach together with empirical results in the literature. Four types of potentials can be distinguished. The first ones are the Lennard–Jones potentials established by Maruyama and Kimura [7] and by Spijker et al. [8]. They depict a relatively weak value of V_e, close to −40 meV, and a short equilibrium $z_e < 3$ Å. The second group of potentials includes those of Head-Gordon et al. [9] and Svanberg and Pettersson [10]. They reproduce correctly the experimental value of V_e, but with relatively large values of z_e compared with the other potentials. Additionally, we can mention the potential of Yamamoto [11], based on the parameters derived by Head-Gordon et al. [9], but with $2\sigma = 3.2\,\text{Å}^{-2}$ instead of $2\sigma = 1.6\,\text{Å}^{-2}$. The resulting potential depicts a weak value for V_e and a relatively large equilibrium distance. The third group concerns the potentials deduced by Smith et al. [12] and Lahaye et al. [13]. Both use global van der Waals attractive part of the potential between Ar and the Pt surface. They are not decomposed into a pairwise sum. The corresponding V_e are lower than −100 meV and the z_e are ≈ 3 Å.

The last group includes the present potential, and those of Kulginov et al. [5] and Ramseyer et al. [6]. Our V_e value well reproduces the experimental value of approximately −80 meV. It is also ranged between the Kulginov and Ramseyer potentials. The $z_e = 3.35$ Å deduced from our potential is also consistent with those of about 3.25 Å from the Kulginov or Ramseyer potentials. Experimentally, no information exists about the equilibrium distance between the Ar atom and the Pt surface but, such values around 3.2 and 3.4 Å should be correct since the last group of potentials reproduce properly as well the experimental equilibrium interaction energy as the experimental vertical Pt(111)–Ar harmonic vibrational frequency. The values of ω_e of this group of potentials are indeed very close to the experimental value of 5 meV [14].

The empirical pairwise potential derived by Kulginov et al. [5] has the form

$$V^{\mathrm{Pt-Ar}}(r_{\mathrm{Pt-Ar}}) = V_0 e^{-\alpha(r_{\mathrm{Pt-Ar}}-r_0)} - \frac{C_6}{r^6_{\mathrm{Pt-Ar}}} \tag{2}$$

with the following parameters $V_0 = 20,000$ eV, $\alpha = 3.3\,\text{Å}^{-1}$, $r_0 = -0.75$ Å, and $C_6 = 68.15\,\text{eV Å}^6$. As it includes the long-range interaction between atoms and agrees quite well with the ab initio results, it will be used in the MD simulation.

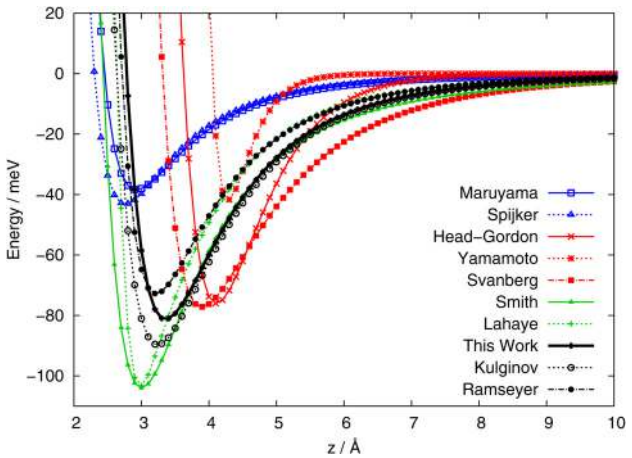

Fig. 1 Pt(111)–Ar interaction potentials

Table 1 Equilibrium interaction energy (V_e in meV), equilibrium distance (z_e in Å), and estimated vertical harmonic vibrational frequency (ω_e in meV) of the Pt(111)–Ar interaction potentials

Potential	V_e/meV	z_e/Å	ω_e/meV
Present	−81.3	3.35	4.8
Kulginov et al. [5]	−89.7	3.24	4.8
Ramseyer et al. [6]	−72.8	3.22	5.0
Maruyama and Kimura [7]	−38.4	2.93	3.9
Spijker et al. [8]	−43.2	2.76	8.1
Head-Gordon et al. [9]	−76.0	4.11	5.7
Svanberg and Pettersson [10]	−77.2	3.89	4.4
Yamamoto [11]	−41.8	4.28	8.8
Smith et al. [12]	−104.0	3.00	5.6
Lahaye et al. [13]	−103.4	2.98	8.7
Exp. [9,14]	−80.0[a]		5.0[b]

[a]Estimated V_0 value.
[b]Anharmonic vibrational frequency.

3 Surface Anisotropy and Directional Accommodation Coefficients

3.1 Atomistic Wall Models. In terms of the potential between the Pt atoms, the multibody quantum Sutton-Chen [15] potential is used. For a system of N Pt-atoms, the potential is given by the following expression:

$$V_{\mathrm{pot,Pt}} = \varepsilon_{\mathrm{Pt}} \left[\frac{1}{2} \sum_{i=1}^{N} \sum_{\substack{j=1 \\ j\neq i}}^{N} \left(\frac{a}{r_{ij}} \right)^{11} - c \sum_{i=1}^{N} \rho_i^{1/2} \right],$$
$$\rho_i = \sum_{\substack{j=1 \\ j\neq i}}^{N} \left(\frac{a}{r_{ij}} \right)^{7} \tag{3}$$

where a is the lattice constant, r_{ij} the distance between atom i and j and the local electron density ρ_i of atom i. The parameters ε, a, c are given as follows: $\varepsilon_{\mathrm{Pt}} = 9.7894 \times 10^{-3}$ eV, $c = 71.336$, $a = 3.9163$ Å.

In this work, two types of surfaces are considered: smooth surfaces and periodic nanotextured surfaces. The orientation of their free surfaces is (100) according to the Miller index. Initially, the Pt atoms are arranged in layers and the two lowest ones are used to fix the system and for the thermostat purpose. The remaining Pt atoms are free to interact with other solid atoms and gas atoms.

A smooth surface model is a system composed of 768 atoms arranged in six layers, all of which are in perfect crystal order. The nanotextured models are constructed from the smooth surface model by adding successively atom layers to create pyramids with the slope angle 45 deg. The base of the pyramid is an infinite strip (Fig. 2), so that anisotropic effects can be considered. In this

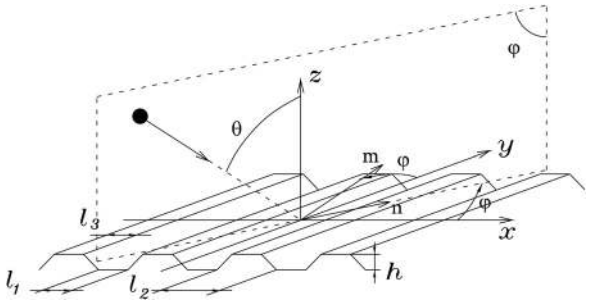

Fig. 2 Nanotextured surface with strips and gas beaming direction θ, φ in cartesian coordinate system. The geometric parameters are $l_1 = 11.76$ Å, $l_2 = 19.6$ Å, $l_3 = 7.84$ Å, $h = 0 - 5.88$ Å.

work, the highest peak, varying with the number of atoms layers added on the surfaces, ranges from 2 to 6 Å.

3.2 MD Simulation of Gas/Wall Collision. The simulations are three-dimensional [16,17]: an Ar atom is projected into a Pt(100) surface with different incident angles θ and with different approaching φ-planes. In spherical coordinate system, (θ, φ) are the polar and azimuthal angles, respectively (see Fig. 2). The directional TMAC $\sigma_t^{dir}(\theta, \varphi)$ is given by

$$\sigma_t^{dir}(\theta, \varphi) = \frac{\langle v_{in} \rangle - \langle v_{rn} \rangle}{\langle v_{in} \rangle} \tag{4}$$

where v_{in} and v_{rn} are the projections of the incident and the reflected velocities on the vector $\mathbf{n}$, respectively. The averages $\langle v_{in} \rangle, \langle v_{rn} \rangle$ in Eq. (4) are taken over a large number of collisions. The approach is similar to Refs. [17,18] but here we also consider the dependence of azimuthal angle for anisotropic surfaces.

We assume first that an Ar atom only interacts with the Pt wall within a cut-off distance $r_c = 10$ Å, which is higher than the common value, around 8.5 Å, used by MD simulations of argon. Beyond that distance, the potential is less than 1% of its well depth (see Fig. 1) and the interaction is negligible. At the beginning of each simulation, an Ar atom is inserted randomly at the height r_c above the wall surface with initial incident velocity $\mathbf{v}_i$. A collision is considered as finished when the atom bounces back beyond the cut-off distance. Then the reflected velocity $\mathbf{v}_r$ is recorded for the statistical purpose and another Ar atom is reinserted randomly in order to continue the process. After approximately 10,000 collisions (simulations), converged values of σ_t values were assumed to be obtained.

Throughout the simulations, periodic boundary conditions were applied along the x, y directions. At each time step, the velocities and positions of the gas and solid atoms are calculated by the usual Leapfrog–Verlet integration scheme. To control the temperature T_w of the system, the phantom technique is used: the Langevin thermostat [19] is applied to the atom layer above the fixed layer. The motion of an atom i belonging to this layer is governed by the equation

$$m_{si} \frac{d\mathbf{v}_{si}(t)}{dt} = -\xi \mathbf{v}_{si}(t) + \mathbf{f}_i(t) + \mathbf{R}_i(t) \tag{5}$$

In Eq. (5), $\mathbf{v}_{si}$ is the velocity of the atom i, $\mathbf{f}_i$ is the resulting force acting on it by the surrounding ones, m_{si} is the atomic mass, and ξ is the damping coefficient. The third term $\mathbf{R}_i$ in the right hand side of Eq. (5) is the random force applied on the atom. In the simulation, it is sampled after every time step δt from a Gaussian distribution, with zero average and mean deviation of $\sqrt{6\xi k_B T_w / \delta t}$. The simulations were carried out by setting time step and damping factor at the following values:

$$\delta t = 2\text{fs}, \quad \xi = 5.184 \times 10^{-12} \text{ kg/s} \tag{6}$$

The wall temperature T_w was kept at 200 K, 300 K, and 400 K and the gas beam temperature T_g was kept at a slightly higher value than T_w, i.e., $T_g = 1.1 T_w$.

3.3 Results for Anisotropic Surfaces. In the framework of the kinetic theory, Dadzie and Meolans [20] proposed a new scattering kernel that accounts for surface anisotropy. Their formulation is based on three independent accommodation coefficients $\alpha_x, \alpha_y, \alpha_z$ along the three directions x, y, z. The coefficients α_x, α_y represent the tangential accommodation coefficients and α_z is the normal accommodation coefficient. The tangential accommodation coefficient α_n in direction n is then computed by the expression

$$\sigma_t^{an}(\varphi) = \alpha_n = \alpha_x \cos^2 \varphi + \alpha_y \sin^2 \varphi \tag{7}$$

We remark that by substituting $\varphi = 0$ deg and $\varphi = 90$ deg, the accommodation values α_x and α_y along x and y directions can be recovered. In this subsection, we study the anisotropy effect using MD and the directional σ_t definition in Eq. (4) and examine Eq. (7). It is noted that Eq. (7) based on the kinetic theory model is more restrictive than Eq. (4): the accommodation coefficient is independent from the angle θ. MD computation based on Eq. (4) showed that the θ dependency may be significant at high h [16]. As a result, there is no unique way to determine the model parameters in Eq. (7) with Eq. (4). One can determine $\sigma_t^{an}(\varphi)$ by fixing the angle θ or averaging over all possible θ, etc. In this paper, for the modeling purpose, we shall be content with the first method, i.e., calculation of σ_t at $\theta = 45$ deg while assuming that to some extent, σ_t varies little with θ around this mean value.

The anisotropy effect can be seen from Fig. 3: the σ_t^{dir} variation with φ is nonuniform for rough surfaces. The accommodation process along the two directions x, y is highly different. The σ_t^{dir} is minimum when the atoms are projected along the longitudinal direction of the strip ($\varphi = 90$ deg), since the surface may be considered as almost smooth in that direction (see Fig. 2). This σ_t value corresponds to α_y in the model of Ref. [20]. The maximal σ_t values recorded for $\varphi = 0$ deg and $h > 0$ can be attributed to the largest roughness effect in that direction and correspond to α_x in the model [20]. Moreover, Figure 3 shows an increase of anisotropy effect as the roughness increases: the difference between the highest and the smallest σ_t value increases with the roughness height whereas the σ_t results depend very little on the beaming direction for a smooth surface. This could be explained by the fact that the smooth surface can be considered isotropic.

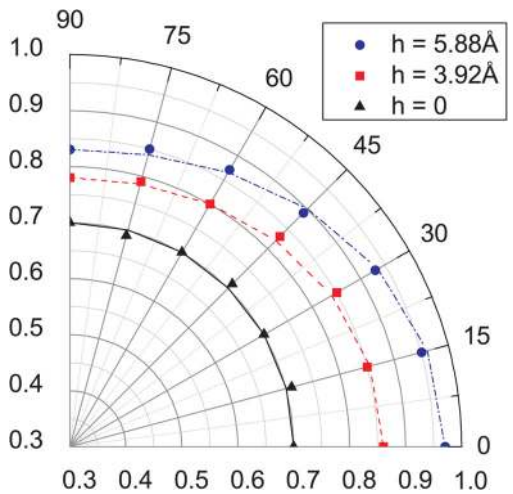

Fig. 3 σ_t^{dir} computed for striped walls versus azimuth angle φ for different roughnesses ($T_w = 300$ K, $\theta = 45$ deg). The solid, dashed, dashed-dotted lines are the analytical expressions (7) used to fit the present numerical results.

For anisotropic surfaces, the reflected flux is not always lying in the same plane as the arriving one. Consequently, in addition to Eq. (4), we should account for the ratio of the reflected flux components along two orthogonal directions m, n: $\langle v_{rm}\rangle/\langle v_{rn}\rangle$. According to the anisotropic model, this ratio can be computed by the expression

$$\langle v_{rm}\rangle/\langle v_{rn}\rangle = \frac{(\alpha_x - \alpha_y)\cos\varphi\sin\varphi}{1 - \alpha_x\cos^2\varphi - \alpha_y\sin^2\varphi} \tag{8}$$

By observing the surface structure, we can deduce that $\langle v_{rm}\rangle/\langle v_{rn}\rangle$ must vanish for impinging fluxes parallel to the planes of symmetry of the anisotropic surface. That remark is in good agreement with Eq. (8) where $\langle v_{rm}\rangle/\langle v_{rn}\rangle = 0$ at $\varphi = 0\,\text{deg}, 90\,\text{deg}$. Our MD simulation confirms this remark and also shows that the ratio is nonzero at $\varphi \neq 0$. Numerical results show that at $\varphi = 45\,\text{deg}$, the ratio is significant and increases from 0 to 0.67 as the roughness height increases, i.e., the anisotropic effect is enhanced.

4 Anisotropic Slippage in Gaseous Flows

4.1 Simplified Slip Model Based on Anisotropic Accommodation Coefficients. The original paper of Dadzie and Meolans [20] showed a linear relationship between the incoming momentum fluxes (Φ_x^+, Φ_y^+) and outgoing tangential momentum fluxes (Φ_x^-, Φ_y^-) at the wall. Since (Φ_x^+, Φ_y^+) and (Φ_x^-, Φ_y^-) are components of tangential momentum vector fluxes $\mathbf{\Phi}_t^+$ and $\mathbf{\Phi}_t^-$ expressed in the same basis, we rewrite the linear relation in tensorial form [21]

$$\mathbf{\Phi}_t^+ = (\mathbf{I} - \mathbf{A})\mathbf{\Phi}_t^- \tag{9}$$

where $\mathbf{I}$ is the identity tensor and $\mathbf{A}$ is the accommodation tensor admitting the diagonal form in the current basis

$$\mathbf{A} = \begin{bmatrix} \alpha_x & 0 \\ 0 & \alpha_y \end{bmatrix} \tag{10}$$

Finally, we note the following relation which results from Eq. (9):

$$(\mathbf{\Phi}_t^+ + \mathbf{\Phi}_t^-) = \mathbf{N}(\mathbf{\Phi}_t^- - \mathbf{\Phi}_t^+), \quad \mathbf{N} = 2\mathbf{A}^{-1} - \mathbf{I} \tag{11}$$

In the current basis Oxy, tensor $\mathbf{N}$ is reduced to the matrix

$$\mathbf{N} = \begin{bmatrix} (2-\alpha_x)/\alpha_x & 0 \\ 0 & (2-\alpha_y)/\alpha_y \end{bmatrix} \tag{12}$$

In what follows, we consider gas flows over a periodic nanotextured surface (see Fig. 2) and assume that it is possible to replace it by a nominally flat surface and an equivalent gas–wall interaction model. The derivation of the following slip model for the equivalent surface relies essentially on the momentum equation and its associated properties in Eqs. (9)–(12). A similar methodology based on the flux approximation can be found in the previous work [21,22] and books on microfluidics [23–25]. We consider a control surface near and parallel to the immobile wall and study the collisions at this surface. During a unit period of time, there are N gas atoms crossing the surface: N^- atoms go downward and N^+ atoms go upward with the tangential velocity $\mathbf{v}_t' = (v_x', v_y')$ and $\mathbf{v}_t = (v_x, v_y)$ (see Fig. 4). The gas velocity $\mathbf{u}_s$ at the wall can be obtained by the average

$$m_g N\mathbf{u}_s = m_g N^+\langle\mathbf{v}_t\rangle + m_g N^-\langle\mathbf{v}_t'\rangle \tag{13}$$

The notation $\langle\,\rangle$ indicates the average over the gas atoms. It is clear that $m_g N^+\langle\mathbf{v}_t\rangle$ and $m_g N^-\langle\mathbf{v}_t'\rangle$ are equivalent to the tangential momentum vector fluxes $\mathbf{\Phi}_t^+$ and $\mathbf{\Phi}_t^-$

$$\mathbf{\Phi}_t^+ = m_g N^+\langle\mathbf{v}_t\rangle, \quad \mathbf{\Phi}_t^- = m_g N^-\langle\mathbf{v}_t'\rangle \tag{14}$$

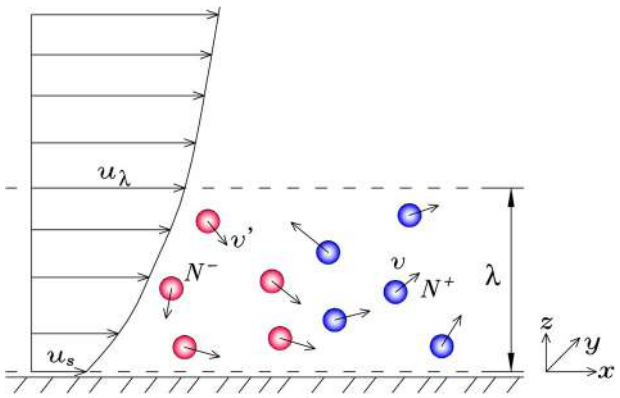

Fig. 4 Collision between gas atoms and a solid wall. The number of gas atoms going downward (velocity v′) and upward (velocity v) within one time unit are denoted N^- and N^+, respectively. If there is no gas accumulation at the wall, $N^+ = N^-$.

Using the linear relation (9) and (13), we can write

$$m_g N\mathbf{u}_s = m_g N^-(2\mathbf{I} - \mathbf{A})\langle\mathbf{v}_t'\rangle \tag{15}$$

Since the velocity of a gas atom is unchanged between collisions, it is possible to think that $\langle\mathbf{v}_t'\rangle$ is equal to the velocity average at one mean free path λ from the wall, hence the stream velocity $\mathbf{u}_\lambda$ at that location. By assuming that $N^- = N^+ = N/2$, the slip velocity $\mathbf{u}_s$ can be deduced as follows:

$$2\mathbf{u}_s = (2\mathbf{I} - \mathbf{A})\mathbf{u}_\lambda \tag{16}$$

We remark that the Taylor development of $\mathbf{u}$ at the wall yields the expression

$$\mathbf{u}_\lambda = \mathbf{u}_s + \lambda\frac{\partial\mathbf{u}}{\partial z} + \frac{\lambda^2}{2}\frac{\partial^2\mathbf{u}}{\partial z^2} + \cdots \tag{17}$$

Considering the first order λ approximation, i.e., $\mathbf{u}_\lambda = \mathbf{u}_s + \lambda(\partial\mathbf{u}/\partial z)$, the final slip equation becomes

$$\mathbf{u}_s = \lambda(2\mathbf{A}^{-1} - \mathbf{I})\frac{\partial\mathbf{u}}{\partial z} = \lambda\mathbf{N}\frac{\partial\mathbf{u}}{\partial z} \tag{18}$$

The term standing before $\partial\mathbf{u}/\partial z$ is equivalent to the slip length tensor $\mathbf{b} = \lambda\mathbf{N}$. The latter can be made dimensionless with a characteristic length, for example the channel height H

$$\frac{\bar{\mathbf{b}}}{\text{Kn}} = \mathbf{N}, \quad \text{with} \quad \text{Kn} = \frac{\lambda}{H} \tag{19}$$

where Kn is the Knudsen number. We must also notice that the slip models are based on the validity of Navier–Stokes–Fourier equations at the wall, which is not true. However, as shown in previous works and from our MD results reported in Sec. 3.2, these models can describe reasonably well the slip effects near the wall. Furthermore, errors can be dealt with using empirical coefficients or higher order models, etc.

4.2 Analytical Solutions for Poiseuille Flows. We consider confined gas flows between two immobile parallel textured walls. The (dimensionless) slip tensors of each wall are denoted, respectively, $\bar{\mathbf{b}}^+$ (upper wall) and $\bar{\mathbf{b}}^-$ (lower wall). The flows can be driven by either pressure difference or body force field. As shown in previous works [22,26–28] relevant to isotropic surfaces, Poiseuille parabolic solution can describe well the velocity profile even in nanosized channels and at high Knudsen numbers. These

results suggest that we can adopt the following equation for the case under consideration [29]:

$$\mathbf{u} = \frac{H^2}{4\eta}\left\{\frac{1}{2}\left[1-\left(\frac{2z}{H}\right)^2\right]\mathbf{I} + \mathbf{J} + \left(\frac{2z}{H}\right)\mathbf{K}\right\}\mathbf{g} \tag{20}$$

with $\mathbf{g}$ being the driving force, equivalent to the pressure gradient or to the body force. Tensors $\mathbf{J}, \mathbf{K}$ are defined by

$$\begin{aligned} &\mathbf{J} = \mathbf{C} - \mathbf{D}(\mathbf{I}+\mathbf{C})^{-1}\mathbf{D}, \quad \mathbf{K} = (\mathbf{I}+\mathbf{C})^{-1}\mathbf{D}, \\ &\mathbf{C} = \bar{\mathbf{b}}^+ + \bar{\mathbf{b}}^-, \quad \mathbf{D} = \bar{\mathbf{b}}^+ - \bar{\mathbf{b}}^- \end{aligned} \tag{21}$$

In the case where the slip tensors $\bar{\mathbf{b}}^+, \bar{\mathbf{b}}^-$ are diagonal in the basis Oxy, $\mathbf{J}, \mathbf{K}$ are also diagonal in the same basis and their components admit the expressions

$$\begin{aligned} J_x &= \frac{\bar{b}_x^+ + \bar{b}_x^- + 4\bar{b}_x^+\bar{b}_x^-}{1+\bar{b}_x^+ + \bar{b}_x^-}, \quad J_y = \frac{\bar{b}_y^+ + \bar{b}_y^- + 4\bar{b}_y^+\bar{b}_y^-}{1+\bar{b}_y^+ + \bar{b}_y^-}, \\ K_x &= \frac{\bar{b}_x^+ - \bar{b}_x^-}{1+\bar{b}_x^+ + \bar{b}_x^-}, \quad K_y = \frac{\bar{b}_y^+ - \bar{b}_y^-}{1+\bar{b}_y^+ + \bar{b}_y^-} \end{aligned} \tag{22}$$

If Eq. (19) holds, we can rewrite the previous expressions as follows:

$$\begin{aligned} J_x &= \frac{\mathrm{Kn}(N_x^+ + N_x^-) + 4\mathrm{Kn}^2 N_x^+ N_x^-}{1+\mathrm{Kn}(N_x^+ + N_x^-)}, \\ J_y &= \frac{\mathrm{Kn}(N_y^+ + N_y^-) + 4\mathrm{Kn}^2 N_y^+ N_y^-}{1+\mathrm{Kn}(N_y^+ + N_y^-)}. \\ K_x &= \frac{\mathrm{Kn}(N_x^+ - N_x^-)}{1+\mathrm{Kn}(N_x^+ + N_x^-)}, \\ K_y &= \frac{\mathrm{Kn}(N_y^+ - N_y^-)}{1+\mathrm{Kn}(N_y^+ + N_y^-)} \end{aligned} \tag{23}$$

These analytical expressions will be examined in Sec. 4.4, thanks to the MD method.

4.3 MD Simulation of Gas Flows. In this section, we described the MD method used to simulate gas flows in a nanochannel. The gas atoms are placed in a rectangular box of dimension $L \times B \times H$ along the x, y, z directions and subject to a uniform force field $\boldsymbol{\gamma}$, parallel to the plane xOy, with

$$\mathbf{g} = m_\mathrm{g}\rho_\mathrm{o}\boldsymbol{\gamma} \tag{24}$$

and ρ_o the global number density. We assume that the interaction between the gas atoms and the walls (normal to the z direction) are anisotropic with the following parameters:

$$\alpha_x = 0.96, \quad \alpha_y = 0.83, \quad \alpha_z = 0.9, \quad T_\mathrm{w} = 300\ \mathrm{K} \tag{25}$$

It should be noted that the values of α_x, α_y correspond to the tangential accommodations coefficients for Ar and a nanotextured Pt wall at $T_\mathrm{w} = 300\,\mathrm{K}$ studied in Sec. 3.2. MD simulations also show that results are little sensitive to α_z.

Boundary conditions for MD methods that can mimic the effects of Eq. (9) are implemented. During MD simulations, when a gas atom crosses the wall boundary, we consider that it collides with the wall. Then, the same atom is reinserted at the wall boundary with the same x, y coordinates and its velocity is reassigned on the basis of different elementary processes. At each collision event, a random number X with uniform distribution between $[0,1]$ is generated. Depending on the value of X and the arriving velocity $\mathbf{v}'$, we shall decide the reflection mechanism and generate the post collision velocity $\mathbf{v}$ accordingly, for example:

- If $0 < X < \mu_0$ then the reflection is specular: $v_x = v_x'$, $v_y = v_y'$, $v_z = -v_z'$.
- If $\mu_0 < X < \mu_0 + \mu_{xy}$ then the reflection is specular along z, diffusive along x, y directions: $v_x, v_y \sim \mathcal{N}(0, \sqrt{kT_\mathrm{w}/m_\mathrm{g}})$, $v_z = -v_z'$.
- If $\mu_0 + \mu_{xy} < X < \mu_0 + \mu_{xy} + \mu_{xz}$ then the reflection is specular along y, diffusive along x, z directions $v_x \sim \mathcal{N}(0, \sqrt{kT_\mathrm{w}/m_\mathrm{g}})$, $v_z \sim \mathcal{R}(\sqrt{kT_\mathrm{w}/m_\mathrm{g}})$ and $v_y = v_y'$.
- If $\mu_0 + \mu_{xy} + \mu_{xz} < X < \mu_0 + \mu_{xy} + \mu_{xz} + \mu_{yz}$ then the reflection is specular along x, diffusive along y, z directions $v_y \sim \mathcal{N}(0, \sqrt{kT_\mathrm{w}/m_\mathrm{g}})$, $v_z \sim \mathcal{R}(\sqrt{kT_\mathrm{w}/m_\mathrm{g}})$, and $v_x = v_x'$.
- If $\mu_0 + \mu_{xy} + \mu_{xz} + \mu_{yz} < X < \mu_0 + \mu_{xy} + \mu_{xz} + \mu_{yz} + \mu_x$ then the reflection is specular along y, z, diffusive along x direction $v_x \sim \mathcal{N}(0, \sqrt{kT_\mathrm{w}/m_\mathrm{g}})$, $v_y = v_y'$, and $v_z = -v_z'$.
- If $\mu_0 + \mu_{xy} + \mu_{xz} + \mu_{yz} + \mu_x < X < \mu_0 + \mu_{xy} + \mu_{xz} + \mu_{yz} + \mu_x + \mu_y$ then the reflection is specular along x, z, diffusive along y direction $v_y \sim \mathcal{N}(0, \sqrt{kT_\mathrm{w}/m_\mathrm{g}})$, $v_x = v_x'$, and $v_z = -v_z'$.
- If $\mu_0 + \mu_{xy} + \mu_{xz} + \mu_{yz} + \mu_x + \mu_y < X < \mu_0 + \mu_{xy} + \mu_{xz} + \mu_{yz} + \mu_x + \mu_y + \mu_z$ then the reflection is specular along x, y, diffusive along z direction $v_z \sim \mathcal{R}(\sqrt{kT_\mathrm{w}/m_\mathrm{g}})$, $v_x = v_x'$ and $v_y = v_y'$.
- If $\mu_0 + \mu_{xy} + \mu_{xz} + \mu_{yz} + \mu_x + \mu_y + \mu_z < X < \mu_0 + \mu_{xy} + \mu_{xz} + \mu_{yz} + \mu_x + \mu_y + \mu_z + \mu_{xyz} = 1$ then the reflection is diffusive along x, y, z directions $v_x, v_y \sim \mathcal{N}(0, \sqrt{kT_\mathrm{w}/m_\mathrm{g}})$ and $v_z \sim \mathcal{R}(\sqrt{kT_\mathrm{w}/m_\mathrm{g}})$.

It should be noted that the total sum of the μ_i equals 1 and they are related to α_x, α_y and α_z.

$$\begin{aligned} &\mu_{ij} = \alpha_i\alpha_j(1-\alpha_k), \quad \mu_i = \alpha_i(1-\alpha_j)(1-\alpha_k), \\ &\mu_{ijk} = \alpha_i\alpha_j\alpha_k, \quad \mu_0 = (1-\alpha_i)(1-\alpha_j)(1-\alpha_k), \\ &i,j,k = x,y,z, \quad i \neq j \neq k \neq i \end{aligned} \tag{26}$$

Here $\mathcal{N}(0, \sqrt{kT_\mathrm{w}/m_\mathrm{g}})$ is the normal distribution with zero mean and standard deviation $\sqrt{kT_\mathrm{w}/m_\mathrm{g}}$, and $\mathcal{R}(\sqrt{kT_\mathrm{w}/m_\mathrm{g}})$ is the Rayleigh distribution with parameter $\sqrt{kT_\mathrm{w}/m_\mathrm{g}}$. In addition to the previously described wall boundary conditions along the z direction, the simulation box is periodic along the x, y directions.

It is clear that the described anisotropic collision mechanism is a generalization of Maxwell's original isotropic reflection mechanism. Here, the specular and diffusion reflections are applied to the three velocity components for different proportions of atom μ_i, in order to reproduce the momentum relative changes of Eq. (9). Furthermore, due to a considerable portion of atoms reflecting diffusively at the wall temperature T_w, these boundary conditions correspond to a thermal wall allowing full energy exchange. As a result, thermostats are no longer needed during MD simulation. A rather similar thermal wall approach can be found in Refs. [30,31] concerning the implementation of isotropic Maxwell's model. The use of thermal walls avoids the explicit description of solid wall atoms and reduces considerably the computational cost. The approach is also comparable to classical kinetic gas simulation methods like Boltzmann-based equations [23–25], direct simulation Monte Carlo [32], etc. However, the present MD approach is also capable of simulating the atomic collisions in a deterministic way and flows at large range of gas density. In our simulations, the interaction force between two gas atoms at distance r is governed by the Lennard–Jones potential

$$V(r) = 4\varepsilon\left[\left(\frac{\sigma}{r}\right)^{12} - \left(\frac{\sigma}{r}\right)^{6}\right] \tag{27}$$

with a cutoff distance $r_c = 2.5\sigma$. For Argon, the reference energy ε and length σ are, respectively, $\varepsilon = 1.67 \times 10^{-21}$ J and $\sigma = 3.41$ Å. The global number density is kept constant, $\rho_o = 0.035\sigma^{-3}$ while the number of atoms N, the acceleration γ, and other geometric parameters like L, B, H are changed as shown in Table 2.

During the simulations, the Leapfrog–Verlet integration algorithm is employed and the averaging procedure starts only when the flow is stabilized, i.e., after about 10^6 time steps of 2 fs. The total computational time is 2×10^8 time steps. The height of the channel is divided into 100 layers to determine accurately the distribution of local streamwise velocity $\mathbf{u}$. The flow direction determined by the angle φ made between the flow direction n (also the direction of $\boldsymbol{\gamma}$) and the x axis is also varied from 0 deg to 90 deg to examine the anisotropy effect of the channel. The global mean free path λ used in the analysis is calculated by the formula

$$\lambda = \frac{1}{\sqrt{2}\pi\rho_o\sigma^2} \tag{28}$$

4.4 Results. We consider the case where the two walls are identical and aligned, $\bar{\mathbf{b}}^+ = \bar{\mathbf{b}}^- = \bar{\mathbf{b}}$. This simplification leads to the following expressions of $\mathbf{J}$ and $\mathbf{K}$:

$$\mathbf{J} = 2\bar{\mathbf{b}}, \quad \mathbf{K} = \mathbf{0} \tag{29}$$

The MD simulation results confirm the parabolic velocity profile along the flow direction for most part of the channel, as predicted by Eq. (20). Another interesting aspect that agrees with Eq. (20) and with some previous studies [33,34] is that we observe the occurrence of a small transversal velocity profile. It seems to vanish at principal directions $\varphi = 0\,\text{deg}, 90\,\text{deg}$ and it is maximal at $\varphi = 45$ deg (see Fig. 5). We will show that these properties cannot be recovered when the isotropic slip theory is invoked.

Next let us look further into the quantitative aspect of the results. The velocity profiles along the flow direction and the transversal direction are fitted, respectively, with parabolic and constant equation to determine the *fitted* slip velocities at the walls. These numerically computed values will be compared with the analytical solution (Eq. (20)) when Eqs. (19) and (23) are accounted for. We remark that some deviations from the analytical solution are observed in a small region near the wall (the Knudsen layer). We remark also that the *real* slip velocities can be different from the *fitted* velocities. The former are computed directly by averaging molecular velocity before and after collisions with the walls, also considered in this work. However, for the sake of convenience, the terminology "slip velocities" without prefix (*fitted* or *real*) is used to refer to the *fitted* velocities when no comparison is made between these two quantities. According to Eq. (20), the dependence of dimensionless slip lengths on the flow orientation can be expressed by the relation

$$\frac{L_s(\varphi)}{H} = \bar{b}_x \cos^2\varphi + \bar{b}_y \sin^2\varphi \tag{30}$$

or by

$$\frac{L_s(\varphi)}{H} = \text{Kn}\left(\frac{2-\alpha_x}{\alpha_x}\cos^2\varphi + \frac{2-\alpha_y}{\alpha_y}\sin^2\varphi\right) \tag{31}$$

if the simplified quantitative relation (19) is used. From Fig. 6, both analytical solutions and numerical solutions at different Kn show the same trend of L_s in function of φ. All MD data can be fitted perfectly with Eq. (30), showing excellent agreement with the tensorial slip theory. On the other hand, Eq. (31) based on the quantitative estimation of $\bar{b}_x, \bar{b}_y$ shows good agreement with MD results in slip flow regime Kn < 0.1, average error being less than 5%. At higher Kn, considerable discrepancy is observed. The former have been reported in numerous works concerning the original Maxwell slip model and different correction coefficients (either empirically or theoretically based) have been proposed to deal with these issues [23,26,35].

Regarding the ratio between the slip velocities in transverse and longitudinal directions, u_{sm}/u_{sn}, its dependency on the flow direction is given in Eq. (20).

$$\frac{u_{sm}}{u_{sn}} = \frac{(\bar{b}_y - \bar{b}_x)\sin\varphi\cos\varphi}{\bar{b}_x\cos^2\varphi + \bar{b}_y\sin^2\varphi} \tag{32}$$

using $\bar{b}_x, \bar{b}_y$ parameters from the fit of L_s in Eq. (30), or

$$\frac{u_{sm}}{u_{sn}} = \frac{\left(\dfrac{2-\alpha_y}{\alpha_y} - \dfrac{2-\alpha_x}{\alpha_x}\right)\sin\varphi\cos\varphi}{\dfrac{2-\alpha_x}{\alpha_x}\cos^2\varphi + \dfrac{2-\alpha_y}{\alpha_y}\sin^2\varphi} \tag{33}$$

Table 2 Input data of MD simulations in reduced unit. For Argon, $\sigma = 3.41$ Å and $\varepsilon/m_g\sigma = 7.323\times10^{13}$ m/s^2.

N(atoms)	$L(\sigma)$	$B(\sigma)$	$H(\sigma)$	Kn	$\gamma(\varepsilon/m\sigma)$
74,088	128.4	128.4	128.4	0.050	0.001
27,000	91.7	91.7	91.7	0.070	0.001
8000	61.1	61.1	61.1	0.104	0.001
4400	61.1	61.1	33.6	0.190	0.001

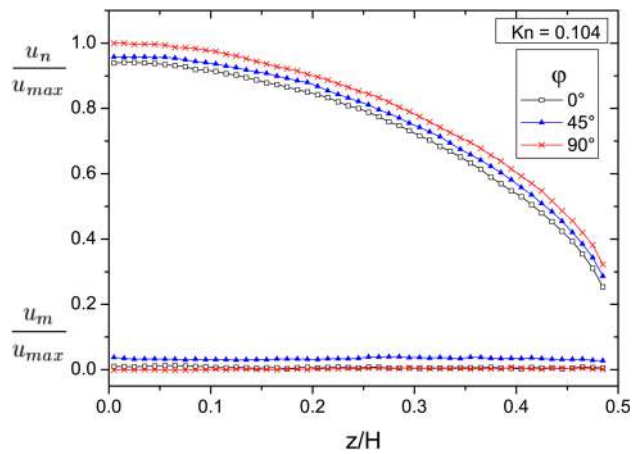

Fig. 5 Longitudinal and transverse velocity profiles u_n, u_m for different values of φ and Kn = 0.104. The velocities are normalized with u_{max}—the velocity at $z = 0$ for case $\varphi = 90$ deg .

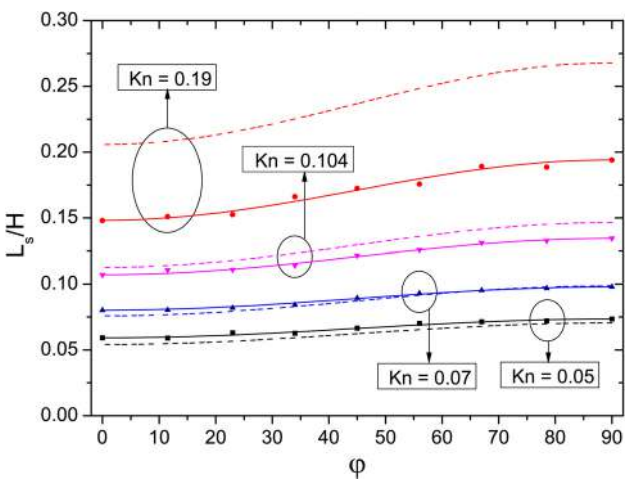

Fig. 6 Dimensionless slip length L_s/H as a function of φ at different Kn. Points are MD data which are fitted with solid lines corresponding to the analytical expression (30). The dashed lines represent quantitative estimation (31) based on α_x, α_y .

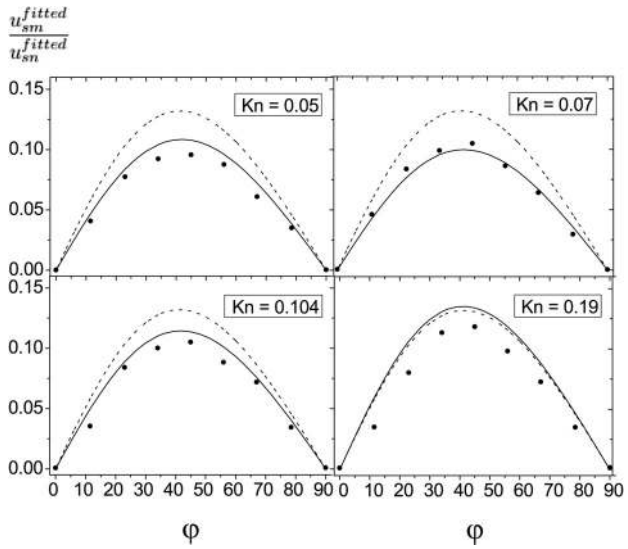

Fig. 7 Ratio of transverse and longitudinal components of fitted slip velocity as a function of φ for various Kn. Points are MD data, the solid and dashed lines are analytical expressions (32) and (33).

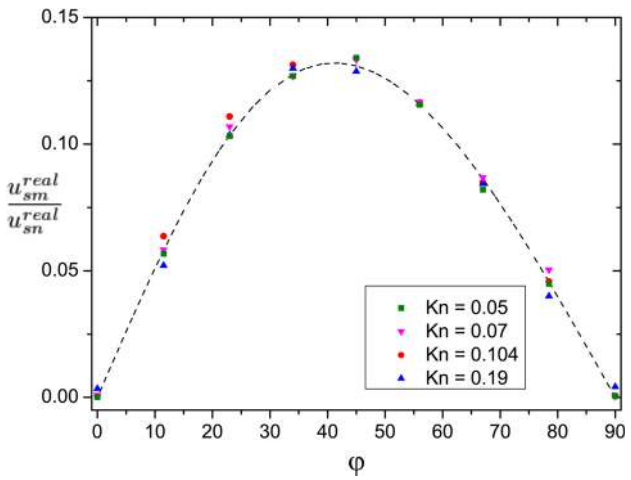

Fig. 8 Ratio of transverse and longitudinal components of real slip velocity as a function of φ for different Kn. Points are MD data and the dashed line is for the analytical expression (33).

using the approximation given in Eq. (19). It is clear that this ratio always vanishes by assuming isotropy. For anisotropic surfaces, it is a function of φ and only vanishes when $\varphi = 0\,\text{deg}, 90\,\text{deg}$.

Figure 7 shows *fitted* slip velocities obtained from MD simulations in comparison with analytical predictions of Eqs. (32) and (33). Again, MD results agree very well with the analytical expression given in Eq. (32) and less well with the quantitative expression given by Eq. (33). More precisely, Equation (33) overestimates the *fitted* transverse flow velocity. However, when we look into the *real* slip velocities in Fig. 8, there is a very good agreement and, more interestingly, the ratio is quasi independent of Kn, as predicted in Eq. (33).

5 Conclusions

We have presented a three-step approach to study the directional dependence of slip effects for gas flows: determination of the gas–wall potential, simulation and modeling of the gas–wall collisions, simulation and modeling of the anisotropic slip effects. The present multiscale methodology combines the advantages of the DFT method, the MD method and gas–wall interface model in the kinetic theory. The DFT method is used to compute precisely the interaction potential from the first principle and the electronic structure of the material. The MD method uses the explicit interaction between the atoms to simulate realistic fluid flows. The studies of gas–wall collisions, the equivalent collision model, and its effect on the macroscopic scale are interesting from both theoretical and practical aspects. In particular, the use of gas–wall collision model reduces considerably the computational cost, enabling realistic gas simulations with the MD method. The main concluding remarks drawn from this study are as follows:

(a) The ab initio-based results including equilibrium distance and adsorption energy are in good agreement with empirical results reported in the literature (see Sec. 2). Consequently, it is shown that the gas–wall potential can be expanded in pairwise contributions according to the approach by Kulginov et al. [5]. Therefore, it has been used for the MD simulations.

(b) The angular dependence of the TMAC is computed and analyzed in comparison with isotropic/anisotropic scattering kernel models. It is shown that the extension of the Maxwell model, Eq. (7), can describe quite well anisotropic slip effects if two TMAC parameters are used.

(c) Anisotropic effects on TMAC increase as the roughness increases. For example, the numerical results show that at the azimuthal angle $\varphi = 45\,\text{deg}$, the anisotropic effect enhances the ratio of the reflected velocity components along two orthogonal directions from 0 to 0.67 as the roughness height increases. This effect agrees with the theoretical prediction presented in Eq. (8).

(d) The MD simulation results confirm that the velocity profile is parabolic along the flow direction in most part of the channel. However, the anisotropic slip theory shows occurrence of a small transversal velocity component, maximal at $\varphi = 45\,\text{deg}$, and very weak in the principal flow direction, i.e., $\varphi = 0\,\text{deg}, 90\,\text{deg}$ (see Fig. 5).

(e) Analytical solutions and numerical solutions at different Kn show the same trend on L_s in function of φ. All MD data show excellent agreement with the tensorial slip theory. At higher Kn, considerable discrepancy is observed, as it has been previously reported in the literature (see Fig. 6).

(f) The MD results agree also very well with an analytical expressions (32), (33) which predict the ratio between slip velocities in transverse and longitudinal directions as a function of φ and the slip tensor coefficients.

Nomenclature

a = quantum Sutton–Chen potential parameter
$\mathbf{A}$ = accommodation tensor
$\mathbf{b}, \overline{\mathbf{b}}$ = slip length tensors
c = quantum Sutton–Chen potential parameter
$\mathbf{C}, \mathbf{D}$ = tensors in Poiseuille solution
D_e = dissociation energy parameter
$\mathbf{g}$ = driving force
$\mathbf{J}, \mathbf{K}$ = flow tensors
L, B, H = length, width, and height of the channel
L_s = slip length
l_1, l_2, l_3 and h = geometric parameters of the nanotextured surface
k_B = Boltzmann constant
Kn = Knudsen number
m, n = direction indices
m_g, m_s = masses of the gas and solid atoms
N = number of molecules
$\mathbf{N}$ = accommodation tensor in the current basis Oxy
r_c = cut-off radius
r_{ij} = distance between particles i and j
t = time variable
T_g, T_w = gas and wall temperatures

$\mathbf{u}$ = stream velocity
u_n, u_m = longitudinal and transverse velocity
u_{sn}, u_{sm} = longitudinal and transverse slip velocity
V, V_e = potential energy
$\mathbf{v}_i$, $\mathbf{v}_r$ = incident and reflected velocity
X = random number
(x, y, z) = Cartesian coordinate
α_x, α_y, α_z = accommodation coefficients along x, y, z
$\boldsymbol{\gamma}$ = gravity-like force field
ε = potential parameter
η = viscosity
θ, φ = zenithal and azimuthal angles
λ = mean free path
μ_i = percentage of reflection mechanism i
ξ = damping coefficient
ρ = global number density
ρ_i = local density of atom i
σ = potential parameter
σ_t = tangential momentum accommodation coefficient
$\mathbf{\Phi}_t^-$, $\mathbf{\Phi}_t^+$ = incoming and outcoming tangential momentum flux at the wall
ω = vertical harmonic vibrational frequency

References

[1] Dovesi, R., Orlando, R., Civalleri, B., Roetti, C., Saunders, V. R., and Zicovich-Wilson, C. M., 2005, "Crystal: A Computational Tool for the ab Initio Study of the Electronic Properties of Crystals," Z. Kristallogr., **220**, pp. 571–573.

[2] Léonard, C., Brites, V., Pham, T. T., To, Q. D., and Lauriat, G., 2013, "Influence of the Pairwise Potential on the Tangential Momentum Accommodation Coefficient: A Multi-Scale Study Applied to the Argon on Pt(111) System," Eur. Phys. J. B, **86**.

[3] Doll, K., 2004, "CO Adsorption on the Pt (111) Surface: A Comparison of a Gradient Corrected Functional and a Hybrid Functional," Surf. Sci., **573**(3), pp. 464–473.

[4] Nada, R., Nicholas, J. B., McCarthy, M. I., and Hess, A. C., 1996, "Basis Sets for ab Initio Periodic Hartree-Fock Studies of Zeolite/Adsorbate Interactions: He, Ne, and Ar in Silica Sodalite," Int. J. Quantum Chem., **60**(4), pp. 809–820.

[5] Kulginov, D., Persson, M., Rettner, C. T., and Bethune, D. S., 1996, "An Empirical Interaction Potential for the Ar/Pt (111) System," J. Chem. Phys., **100**(19), pp. 7919–7927.

[6] Ramseyer, C., Hoang, P. N. M., and Girardet, C., 1994, "Interpretation of High-Order Commensurate Phases for an Argon Monolayer Adsorbed on Pt(111)," Phys. Rev. B, **49**, pp. 2861–2868.

[7] Maruyama, S., and Kimura, T., 1999, "A Study on Thermal Resistance Over a Solid–Liquid Interface by the Molecular Dynamics Method," Therm. Sci. Eng., **7**, pp. 63–68.

[8] Spijker, P., Markvoort, A. J., Nedea, S. V., and Hilbers, P. A. J., 2010, "Computation of Accommodation Coefficients and the Use of Velocity Correlation Profiles in Molecular Dynamics Simulations," Phys. Rev. E, **81**(1), p. 011203.

[9] Head-Gordon, M., Tully, J. C., Rettner, C. T., Mullins, C. B., and Auerbach, D. J., 1991, "On the Nature of Trapping and Desorption at High Surface Temperatures. Theory and Experiments for the Ar–Pt (111) System," J. Chem. Phys., **94**(2), pp. 1516–1527.

[10] Svanberg, M., and Pettersson, J. B. C., 1996, "Survival of Noble Gas Clusters Scattering From Hot Metal Surfaces," Chem. Phys. Lett., **263**(5), pp. 661–666.

[11] Yamamoto, K., 2002, "Slip Flow Over a Smooth Platinum Surface," JSME Int. J. Ser. B, **45**(4), pp. 788–795.

[12] Smith, R. J., Kara, A., and Holloway, S., 1993, "A Molecular Dynamics Study for the Trapping and Scattering of Ar/Pt(111)," Surf. Sci., **281**(3), pp. 296–308.

[13] Lahaye, R. J. W. E., Stolte, S., Kleyn, A. W., Smith, R. J., and Holloway, S., 1994, "Site Dependent Energy Loss in Ar Scattering From Pt(111)," Surf. Sci., **307–309**, pp. 187–192.

[14] Zeppenfeld, P., Becher, U., Kern, K., David, R., and Comsa, G., 1990, "Van Hove Anomaly in the Phonon Dispersion of Monolayer Ar/Pt (111)," Phys. Rev. B, **41**(12), pp. 8549–8552.

[15] Sutton, A. P., and Chen, J., 1990, "Long-Range Finnis–Sinclair Potentials," Philos. Mag. Lett., **61**(3), pp. 139–146.

[16] Pham, T. T., To, Q. D., Lauriat, G., Léonard, C., and Hoang, V. V., 2012, "Effects of Surface Morphology and Anisotropy on the Tangential-Momentum Accommodation Coefficient Between Pt(100) and Ar," Phys. Rev. E, **86**, p. 051201.

[17] Finger, G. W., Kapat, J. S., and Bhattacharya, A., 2007, "Molecular Dynamics Simulation of Adsorbent Layer Effect on Tangential Momentum Accommodation Coefficient," ASME J. Fluid Eng., **129**(1), pp. 31–39.

[18] Rettner, C. T., 1998, "Thermal and Tangential-Momentum Accommodation Coefficients for N_2 Colliding With Surfaces of Relevance to Disk-Drive Air Bearings Derived From Molecular Beam Scattering," IEEE Trans. Magn., **34**(4), pp. 2387–2395.

[19] Schlick, T., 2010, *Molecular Modeling and Simulation: An Interdisciplinary Guide*, Springer, New York.

[20] Dadzie, S. K., and Méolans, J. G., 2004, "Anisotropic Scattering Kernel: Generalized and Modified Maxwell Boundary Conditions," J. Math. Phys., **45**(5), p. 1804.

[21] Pham, T. T., To, Q. D., Lauriat, G., and Léonard, C., 2013, "Tensorial Slip Theory for Gas Flows and Comparison With Molecular Dynamics Simulations Using an Anisotropic Gas–Wall Collision Mechanism," Phys. Rev. E, **87**, p. 053012.

[22] To, Q. D., Bercegeay, C., Lauriat, G., Léonard, C., and Bonnet, G., 2010, "A Slip Model for Micro/Nano Gas Flows Induced by Body Forces," Microfluid. Nanofluid., **8**(3), pp. 417–422.

[23] Karniadakis, G., Beskok, A., and Aluru, N., 2005, *Microflows and Nanoflows: Fundamentals and Simulation*, Springer, New York.

[24] Struchtrup, H., 2005, *Macroscopic Transport Equations for Rarefied Gas Flows: Approximation Methods in Kinetic Theory*, Springer, Berlin.

[25] Liou, W. W., and Fang, Y., 2005, *Microfluid Mechanics: Principles and Modeling*, McGraw-Hill, New York.

[26] Bhattacharya, D. K., and Lie, G. C., 1989, "Molecular Dynamics Simulations of Nonequilibrium Heat and Momentum Transport in Very Dilute Gases," Phys. Rev. Lett., **62**(8), pp. 897–900.

[27] Morris, D. L., Hannon, L., and Garcia, A. L., 1992, "Slip Length in a Dilute Gas," Phys. Rev. A, **46**(8), pp. 5279–5281.

[28] To, Q. D., Pham, T. T., Lauriat, G., and Léonard, C., 2012, "Molecular Dynamics Simulations of Pressure-Driven Flows and Comparison With Acceleration-Driven Flows," Adv. Mech. Eng., **4**, p. 580763.

[29] Bazant, M. Z., and Vinogradova, O. I., 2008, "Tensorial Hydrodynamic Slip," J. Fluid Mech., **613**, pp. 125–134.

[30] Tehver, R., Toigo, F., Koplik, J., and Banavar, J., 1998, "Thermal Walls in Computer Simulations," Phys. Rev. E, **57**, pp. 17–20.

[31] Bhattacharya, D. K., and Lie, G. C., 1991, "Nonequilibrium Gas Flow in the Transition Regime: A Molecular-Dynamics Study," Phys. Rev. A, **43**(2), pp. 761–767.

[32] Bird, G. A., 1994, *Molecular Gas Dynamics and the Direct Simulation of Gas Flows*, Clarendon, Oxford, UK.

[33] Belyaev, A. V., and Vinogradova, O. I., 2010, "Effective Slip in Pressure-Driven Flow Past Super-Hydrophobic Stripes," J. Fluid Mech., **652**, pp. 489–499.

[34] Priezjev, N. V., 2011, "Molecular Diffusion and Slip Boundary Conditions at Smooth Surfaces With Periodic and Random Nanoscale Textures," J. Chem. Phys., **135**(20), p. 204704.

[35] Albertoni, S., Cercignani, C., and Gotusso, L., 1963, "Numerical Evaluation of the Slip Coefficient," Phys. Fluids, **6**(7), pp. 993–996.